Evolution of the 2021 Outburst of GX 339-4 with *AstroSat*

Vaibhav Sharma,[1]★ Ranjeev Misra,[2] J S Yadav[3,4] Akash Garg[2] Pankaj Jain[1,3]

[1]*Department of Physics, Indian Institute of Technology Kanpur, Kanpur Nagar, Uttar Pradesh 208016, India*
[2]*Inter-University Center for Astronomy and Astrophysics, Ganeshkhind, Pune, Maharashtra 411007, India*
[3]*Space, Planetary and Astronomical Sciences and Engineering, IIT Kanpur, Kanpur Nagar, Uttar Pradesh 208016, India*
[4]*Department of Astronomy and Astrophysics, Tata Institute of Fundamental Research, Mumbai, Maharashtra 400005, India*

ABSTRACT

We present a comprehensive study of the 2021 outburst of GX 339-4 using `AstroSat` observations in the hard-intermediate (HIMS) and soft-intermediate states (SIMS). Spectral and timing analyses across these states suggest that during the SIMS, unabsorbed flux (0.1-3 keV), inner disc temperature, and "apparent" inner disc radius do not change, suggesting the stability of the disc. In the SIMS, the photon index decreases from ~ 2.1 to ~ 1.7, indicating spectral hardening. The power density spectra (PDS) suggest the presence of quasi-periodic oscillations (QPOs) in the HIMS and SIMS. The QPO frequency evolves from ~ 0.1 Hz to ~ 0.2 Hz in the HIMS, and further to ~ 5.7 Hz in the SIMS. We also observe a decrease in QPO frequency from ~ 5.7 Hz to ~ 4.5 Hz during the SIMS. We discuss the evolution of the QPO, fractional root mean square (rms) amplitude, and time-lag spectra. We discover that variations in disc normalization, disc temperature, and coronal heating rate can reproduce the observed rms and lag spectra with a time delay between them.

Key words: X-ray Binaries, Accretion Disc, Data Analysis, Black Hole Physics, X-ray Individual: GX 339-4

1 INTRODUCTION

X-ray binaries (XRBs) are systems consisting of a compact object and a companion star (or donor) orbiting around the center of mass of the combined system. Based on the nature of the compact object, the XRBs are classified into two categories. If the compact object is a neutron star, the system is referred to as a neutron star X-ray binary (NSXB); if the compact object is a black hole, the system is called a black hole X-ray binary (BHXB). The XRBs are further classified into two categories based on the mass of the companion star. If mass of the donor star is $\leq M_{\odot}$, the system is known as a low-mass X-ray binary (LMXB), and if mass of the donor star is $\geq 10\,M_{\odot}$, the system is classified as a high-mass X-ray binary (HMXB).

In general, the black hole (BH) LMXBs exhibit frequent outbursts due to their transient nature. They spend most of their time in quiescence, followed by an outburst that last from a few days to several months (e.g. Dubus et al. 2001; Deegan et al. 2009). A primary cause of the outburst is the change in mass accretion rate, which transitions the source from the quiescence phase to the outburst phase (e.g. Done et al. 2007). During an outburst, both spectral states and temporal properties change. Most of the BH LMXBs follow a q-shaped track in the intensity versus hardness ratio plot during an outburst, commonly known as hardness-intensity diagram (HID; Homan et al. (2001); Belloni et al. 2005; Homan & Belloni 2005), while Tetarenko et al. (2016) and Alabarta et al. (2021) reported that 30-40 % of the total BH LMXBs do not follow the q-shaped track in the HID during their outburst. The intensity in the HID is typically from both thermal and non-thermal emissions, while the hardness ratio (HR2) is defined as the ratio between the intensity of the source in two energy

bands. We define it as the ratio between the intensity of the source in 15-50 keV and 2-20 keV. At the beginning of the outburst, the BH LMXBs are observed in low/hard state (LHS), during which the non-thermal emission dominates. As the outburst progresses, the BH LMXBs transition from the LHS to high/soft state (HSS) through intermediate state (IMS) (Remillard & McClintock 2006). In the HSS, the thermal emission from the accretion disc dominates. The IMS are further categorized into two states: the soft intermediate state (SIMS) and hard intermediate state (HIMS).

X-ray energy spectrum of a BH LMXB can be described by a multi-color disc blackbody and a power law. The multi-color disc blackbody emission is believed to originate from a geometrically thin and optically thick accretion disc (Shakura & Sunyaev 1973). A fraction of disc photons is inverse Comptonized by highly energetic electrons, called the corona, near the BH, producing high-energy tail in the energy spectrum described by the power law (Haardt & Maraschi 1993; Chakrabarti & Titarchuk 1995; Done et al. 2007). The inverse Comptonized photons may be reprocessed in the disc, producing iron K_{α} line around 6.4 keV. Additionally, we may observe a reflection hump at $\sim 20 - 40$ keV, resulting from the reprocessing of inverse Comptonized photons in the disc (Fabian et al. 1989; Matt et al. 1991).

The BHXBs also exhibit X-ray variability in the light curve, which can be seen in the power density spectrum (PDS) as a broad-band noise and sometimes a narrow peaked feature, popularly known as quasi-periodic oscillation (QPO) (Nowak 2000; Belloni et al. 2002; Remillard & McClintock 2006; Ingram & Motta 2019). QPOs are classified as low-frequency QPOs (LFQPO) with frequencies less than 30 Hz and high-frequency QPOs (HFQPO) with frequencies ranging from 30 Hz to a few hundred Hz (Belloni et al. 2012; Méndez et al. 2013; Motta et al. 2022). The LFQPOs are commonly classified
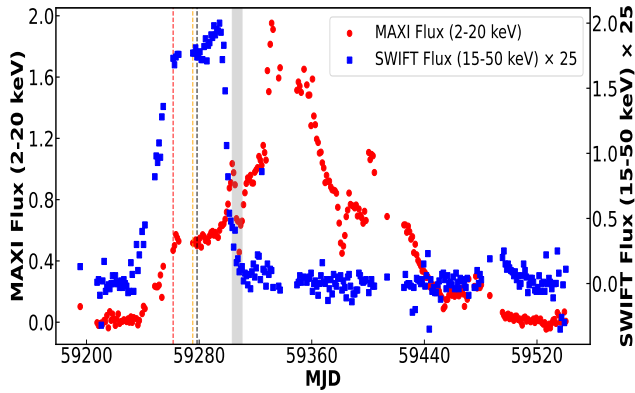
Figure 1. MAXI (2.0–20.0 keV) and Swift/BAT (15.0–50.0 keV) flux light curves of GX 339-4 during its 2021 outburst. The red, orange, and black vertical dashed lines, as well as the dashed grey region indicate the AstroSat observation period. The Swift/BAT flux is scaled by a factor of 25 for comparison.

into three types—A, B, and C (Wijnands et al. 1999; Sobczak et al. 2000; Casella et al. 2005; Motta et al. 2015; Ingram & Motta 2019). Based on their QPO frequency (ν_0), fraction root mean square (rms) amplitude, and quality factor (Q), these types can be characterized as follows: type A ($\nu_0 \sim 8$ Hz, $\leq 3\%$ rms, Q ≤ 3), type B ($\nu_0 \sim 5 - 6$ Hz, $\sim 2 - 4\%$ rms, Q ≥ 6), and type C ($\nu_0 \sim 0.1 - 15$ Hz, $\sim 3 - 16\%$ rms, Q $\sim 7 - 12$) (Casella et al. 2005; Ingram & Motta 2019). The rms amplitude of the QPO is defined as the square root of the normalization of fitted `Lorentzian` component to the QPO, assuming that the PDS is rms-normalized. The quality factor (Q) is defined as the ratio of the QPO frequency ν_0 to its full width at half maximum (FWHM).

Extensive studies have been conducted to investigate the origin of QPOs, but it remains a topic of intense research due to the lack of consensus. Many models have been proposed to explain the origin of QPOs, among which several models consider a geometric origin. Stella & Vietri (1997) and Stella et al. (1999) discuss the relativistic precession model (RPM), which suggests the Lense-Thirring precession as the model for QPO. Ingram et al. (2009) considered the precession of the hot inner flow around the truncated disc (Done et al. 2007) and described this precession as the QPO frequency. A few models, such as Titarchuk & Osherovich (2000), Chakrabarti et al. (2008), Karpouzas et al. (2020), and Bellavita et al. (2022), assume that the QPOs are intrinsic to the accretion flow, arising from instabilities within the accretion flow that lead to quasi-periodic variations in the observed X-ray flux.

The QPO properties evolve as the outburst of the BH LMXB progresses (e.g. Ingram & Motta 2019), and they are tightly correlated with the different spectral states. This suggests that as the spectral properties of the source evolve, the QPO properties also change, indicating correlation between the spectral and temporal properties. Misra & Mandal (2013) discuss a general model to explain the origin by introducing small variations in the spectral properties that characterize the energy spectrum. Maqbool et al. (2019) fit the rms and time-lag spectra of Cyg X-1 with a stochastic propagation model, defined by three parameters: inner disc radius, disc temperature at the truncated radius, and time lag between them.

Garg et al. (2020) also develop a generic model to investigate the responsible radiative component for energy-dependent properties of the QPOs by introducing small amplitude variations in the physical spectral parameters. Garg et al. (2020) assume that the energy spectrum is composed of two components: black body radiation from the accretion disc and inverse Comptonization of the disc photons from the corona. Garg et al. (2022) apply the same model to the QPOs found in MAXI J1535-571, fitting the rms and time-lag spectra by introducing variations in the mass accretion rate ($\dot{m}$), inner disc radius (R_{in}), and coronal heating rate ($\dot{H}$). Using this model, Hussain et al. (2023); Pradhan et al. (2025) reproduce the rms and time lag spectra of the QPO observed in H 1743-322 and MAXI J1803-298, while Dhaka et al. (2024) and Tanenia et al. (2024) fitted the energy-dependent rms and time-lag of the broad feature observed in GRS 1915+105 and GX 339-4, respectively.

BH LMXB GX 339-4 is a well-known source for its frequent outbursts. It is discovered in 1973 by the MIT X-ray detector onboard OSO-7 (Markert et al. 1973), and since then, it has been found to undergo frequent outbursts approximately every 2-3 years. The mass of BH (M_{BH}) in GX 339-4 is still debated, with recent estimates ranging from $7.8 - 10.6 M_\odot$ (Parker et al. 2016), $2.3 - 9.5 M_\odot$ (Heida et al. 2017), to $8.28 - 11.89 M_\odot$ (Sreehari et al. 2019). Hynes et al. (2003) and Heida et al. (2017) suggest lower-bound estimates on the source distance of 6 kpc and 5 kpc, respectively. Zdziarski et al. (2019) determined the M_{BH} of GX 339-4 to be $4 - 11 M_\odot$ using evolutionary models for the donor. They also suggest the inclination angle (i) and the source distance (D) to be $40°$–$60°$ and $8 - 12$ kpc, respectively. In this study, we use averaged values of the M_{BH}, D, and i for GX 339-4, as reported by Zdziarski et al. (2019): $M_{BH} = 7.5 M_\odot$, $D = 10$ kpc, and $i = 50°$, as these represent the latest estimates available.

GX 339-4 underwent an X-ray outburst in 2021, which lasted for approximately ten months. Several X-ray missions observed this source during the outburst, and these observations are studied comprehensively by Wang et al. (2021) (NICER; Arzoumanian et al. 2014; Gendreau et al. 2016), Garcia et al. (2021) (NuSTAR; Harrison et al. 2013), and Liu et al. (2021) (Insight-HXMT; Zhang et al. 2020). AstroSat (Singh et al. 2014) also observed the source during this outburst (Husain et al. 2021; Bhuvana et al. 2021). Multiple observations of AstroSat were made, all during the rising phase of the outburst (Figure 1). The first few observations occurred on February 13, March 02–04, and March 05, 2021, while the last one is an eight-day observation spanning from March 30 to April 06, 2021. Peirano et al. (2022) use the first-day data from the eight-day-long observation to discuss the dual corona comptonization model for type B QPO in GX 339-4. Mondal et al. (2023) and Jana et al. (2024) use the full eight-day data set to discuss the temporal and spectral properties of the source, respectively. Chand et al. (2024) examine the accretion geometry of GX 339-4 in hard states and included data of the observations made on February 13 and March 02, 2021. In a comprehensive spectral and temporal study of the outburst profile of GX 339-4 and H 1743-322, Aneesha et al. (2024) utilize all the data from AstroSat during the 2021 outburst of GX 339-4.

In this work, we include all the observations of AstroSat taken during the 2021 outburst of the GX 339-4. To understand the behaviour of the QPOs, its energy-dependent properties and its correlation with spectral parameters, we extensively study the spectral and temporal evolution of the source during the SIMS and HIMS. We utilize the scheme discussed in Garg et al. (2020) and Garg et al. (2022) to fit the energy-dependent rms and time-lag of the observed QPO to investigate the possible radiative component responsible for changes in the energy-dependent properties of QPO, using the capabilities of the SXT and LAXPC instruments onboard AstroSat.

This paper is organized as follows: Section 2 provides details of the AstroSat observations and the data reduction procedures. Section
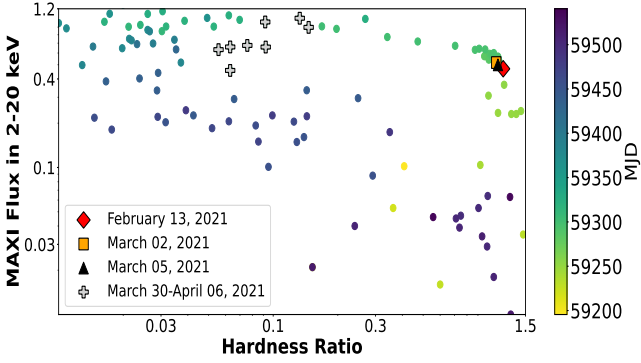
Figure 2. Hardness-Intensity Diagram (HID): The y-axis represents the MAXI flux in the energy range 2-20 keV, while the x-axis shows the HR2, defined as the ratio of Swift/BAT flux in the 15-50 keV range multiplied by 8, divided by the MAXI flux in the 2-20 keV range. The color gradient reflects the time evolution, with the corresponding colorbar displayed on the right side of the figure. Observations O1 (February 13, 2021), O2 (March 02, 2021), and O3 (March 05, 2021) are represented by red diamond, orange square, and black triangle respectively, while O4* and O4 (March 30-April 06, 2021) are represented by gray pluses.

Observation ID	Start Time (MJD)	End Time (MJD)	Exposure Time (ksec)	
			LAXPC	SXT
T03_275T01_9000004180^{O1}	59258.04	59258.82	∼27.04	∼9.49
T03_275T01_9000004218^{O2}	59275.04	59277.77	∼99.44	∼43.23
T03_275T01_9000004222^{†,O3}	59278.05	59278.52	∼14.56	∼2.07
T03_275T01_9000004278^{O4*}	59303.04	59304.16	∼47.65	∼17.89
T03_275T01_9000004278^{O4}	59304.17	59310.86	∼251.58	∼159.81

Table 1. AstroSat Observations of GX 339-4 during the 2021 outburst. † indicates the exposure time of three observation IDs: T03_275T01_9000004222, T03_275T01_9000004224, and T03_275T01_9000004226. We merge them in our analysis as these are on the same day. We define the listed observations as O1, O2, O3, O4*, and O4 (from top to bottom).

3 presents the data analysis, including the light curves, HID, and both spectral (Section 3.1) and timing analysis (Section 3.2). Section 4 discusses the radiative components possibly responsible for the observed QPOs. Finally, Section 5 summarizes our key findings and conclusions.

2 OBSERVATION AND DATA REDUCTION

AstroSat, India's first dedicated astronomy satellite, enables simultaneous multi-wavelength observations of astronomical objects with a single satellite. It is equipped with five payloads covering wavelengths from X-ray to UV. One of the significant payloads on AstroSat is the Large Area X-ray Proportional Counters (LAXPC; Yadav et al. 2016b,a; Agrawal et al. 2017; Antia et al. 2017), which consist of three identical but independent proportional counter units (LAXPC10, LAXPC20, and LAXPC30). Each unit has an effective area of 6000 cm^2 at 15 keV and a time resolution of 10 µs, operating in the energy range of 3.0–80.0 keV. Another important payload is the Soft X-ray Focusing Telescope (SXT; Singh et al. 2016, 2017). The SXT has an effective area of 90 cm^2 at 1.5 keV and a time resolution of 2.4 seconds (full frame) and 0.278 seconds (150 × 150 centered pixel frame), covering the energy range of 0.3–8.0 keV.

The HID is shown in figure 2 using MAXI/GSC (2–20 keV) and Swift/BAT (15–50 keV) flux. We observe that the outburst follows a nearly q-shaped track in the HID. The AstroSat observations are marked in the HID to understand the spectral states of the source during the AstroSat observations.

AstroSat observed the BH LMXB GX 339-4 during its 2021 outburst. The first three observations were conducted on February 13 (O1) (Husain et al. 2021), March 02–04 (O2), and March 05 (O3) (Bhuvana et al. 2021), while the last observation spanned eight days from March 30 to April 06, 2021. To understand the spectral and temporal evolution during the eight-day observation, we divide the data sequentially into twenty segments, each with an exposure of about 13–16 ks. We observe QPOs in the first three segments, whereas the remaining seventeen segments do not show any peaked feature in their PDS. Accordingly, we refer to the first three segments as O4*, where QPOs are present, and the last seventeen segments as O4, where no such feature is observed in the PDS. We further sub-divide the first three segments, now termed as O4*, into fifteen segments, each with an exposure time of ∼ 2500 − 3000 seconds, to study the variations in the QPO frequency and its energy-dependent properties over time. The details of all the observations are provided in Table 1. MAXI flux (2.0–20.0 keV) and normalized Swift/BAT flux (15.0–50.0 keV) are shown in Figure 1 to study the behaviour of soft X-rays and hard X-ray flux during the AstroSat observations. To make the comparison clearer, the Swift/BAT flux is multiplied by 25, allowing its behaviour to be seen alongside the MAXI flux (Figure 1).

Our spectral analysis use data from AstroSat/LAXPC (4.0–25.0 keV in O4* & O4 and 5.0-40.0 keV in O1, O2, and O3 and AstroSat/SXT (0.7–5.0 keV in all the observations) after considering the background domination. Using LAXPC software[1], we create a level2.event.fits file from the level1 data of LAXPC20, which we downloaded from the AstroSat data archive[2] for each observation. Due to low gain and the instrument's response (Antia et al. 2017, 2021), we do not include data from the LAXPC10 and LAXPC30 PCUs in our study. Our analysis focuses on the spectral and temporal properties derived from the level2 data of LAXPC20 only.

We downloaded the SXT level2 data from the AstroSat data archive[3]. To create a merged clean event file, we combine the level2 files of all orbits using the SXT event merger[4] tool in Julia. This merged file is then used to generate light curves and spectra. In the first three listed observations, there is no need for a pile-up correction. During the last eight-day-long observation, the SXT count rate exceeds 40 counts/sec, which is the suggested threshold for pile-up. To mitigate the pile-up effect, we use an annular region with an inner radius of 7 arcmin and an outer radius of 15 arcmin, using the ds9 software. We use the background file 'SkyBkg_comb_EL3p5_Cl_Rd16p0_v01.pha' and the response file 'sxt_pc_mat_g0to12.rmf' provided by the AstroSat science support cell[5]. The vignetting correction is applied using the SXTARFModule_v02 tool[6]. We group the source, response, and background spectrum files using the `ftgrppha` ftool (Kaastra & Bleeker 2016).
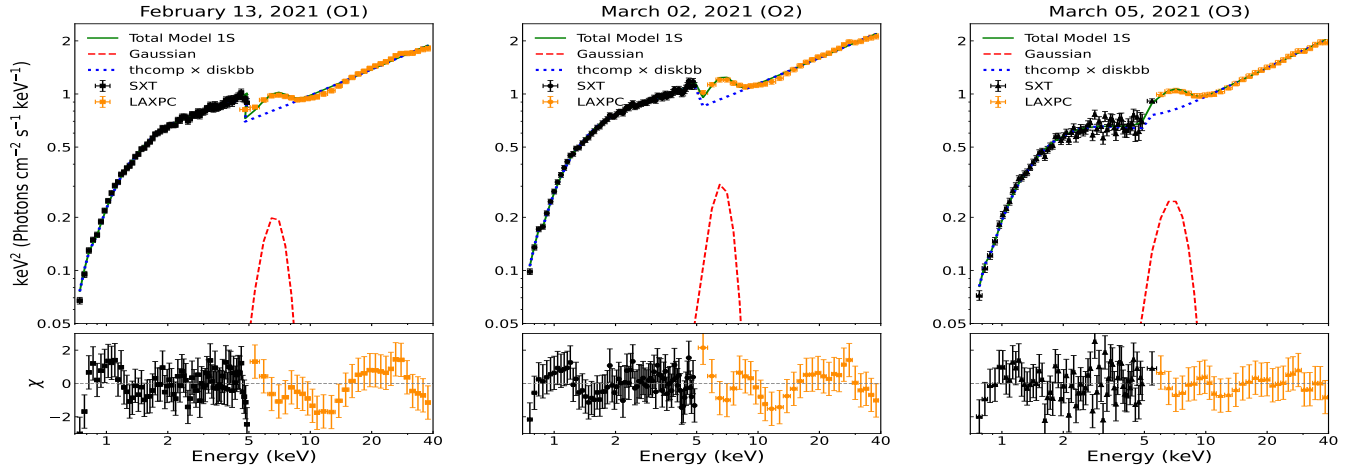

Figure 3. Energy spectrum of observations O1 (Left), O2 (Middle), and O3 (Right), showing SXT (black squares) and LAXPC (orange circles) data points with corresponding error bars. The solid green lines represent the total model fits for each observation, fitted with **Model 1S**. The bottom panel displays the residuals (χ) for each dataset. Individual model components are displayed: Gaussian (dashed red), and thcomp × diskbb (dotted blue).
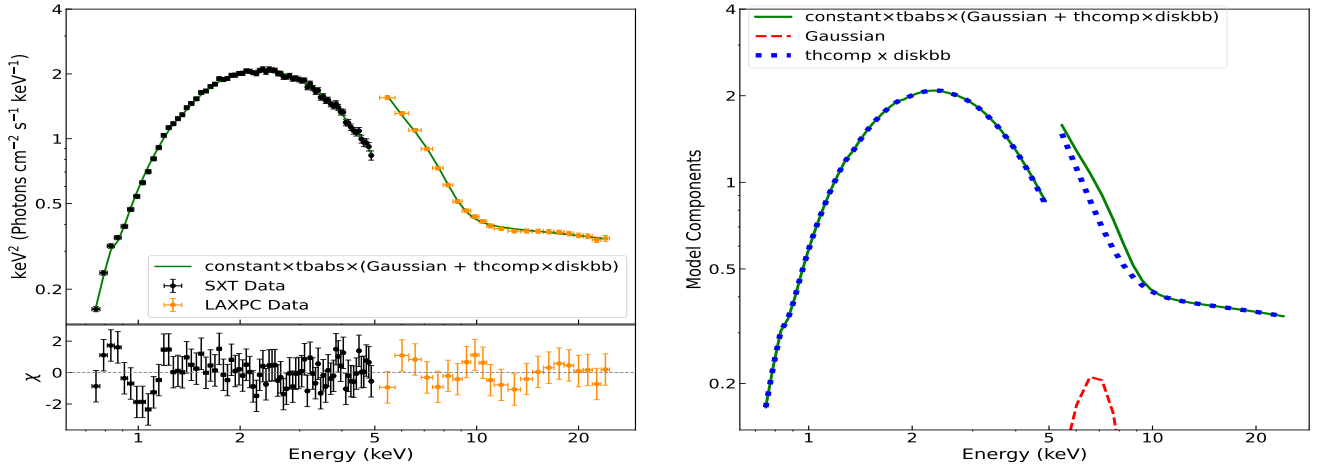

Figure 4. Energy Spectrum and Model Components. **Left Panel:** The upper section shows the observed SXT (black squares) and LAXPC (orange circles) spectra with error bars of segment 1 of O4, overlaid with the best-fit model (solid green line) for **Model 1S:** constant × tbabs × (gaussian + thcomp × diskbb). The lower section presents the residuals (χ) as a function of energy. **Right Panel:** Individual model components are displayed: the total model (solid green), Gaussian (dashed red), and thcomp × diskbb (dotted blue).

3 DATA ANALYSIS

3.1 Spectral Analysis

To study the spectral evolution during the presence of QPOs, we subdivide O4* into fifteen segments (see Section 2 for segmentation details). Similarly, we divide O4 into seventeen segments (see Section 2 for segmentation details) to understand the evolution of the outburst in the absence of QPOs. We perform the spectral analysis on O1, O2, O3, and on the total thirty-two segments of observations O4* and O4.

We begin our spectral analysis with a multi-colour disc blackbody (diskbb; Mitsuda et al. 1984) to model the thermal emission from the accretion disc, and thcomp (Zdziarski et al. 2020) to fit the non-thermal emission. We modify the total model by multiplying a Galactic absorption component tbabs (Wilms et al. 2000), using abund wilm, as recommended in the XSPEC manual. To account for

the differences in the normalization between the SXT and LAXPC instruments, we multiply the total model by a constant factor. The constant factor for LAXPC is fixed at 1, while for SXT, it is kept free. We apply systematic errors of 2% to account for uncertainties in the instrument calibration. We also use the gain fit command within XSPEC to correct for the gain shift in the SXT data during spectral fitting and use the "energies 0.1 300 1000 log" command when applying the **thcomp** model. After fitting the energy spectrum with the above model, residuals indicate that additional fitting, specifically a gaussian component to account for strong residuals around 6.4 keV, is necessary. Therefore, we introduce a gaussian at 6.4 keV.

Thus, the model become *constant* × *tbabs* × *(gaussian + thcomp × diskbb)*, refer to as **Model 1S**. We apply **Model 1S** to all the observations, and we get acceptable fit as we get χ^2_{red} to be 1.03, 0.63, and 0.82 in O1, O2, and O3 respectively (Figure 3) while χ^2_{red} lies between 0.74-1.02 in O4* and 0.53-0.90 in O4. The energy
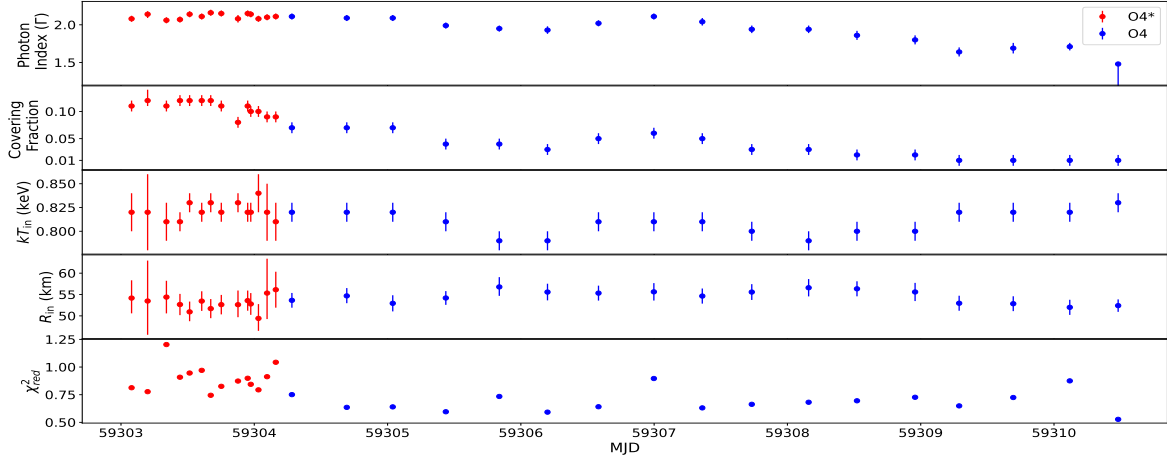
Figure 5. Evolution of the spectral parameters and fit statistics for observations O4* (red) and O4 (blue) as a function of MJD. The panels (top to bottom) show the photon index, covering fraction, inner disc temperature (kT_{in}), apparent inner disc radius, and reduced χ^2 from the spectral fits with **Model 1S**.
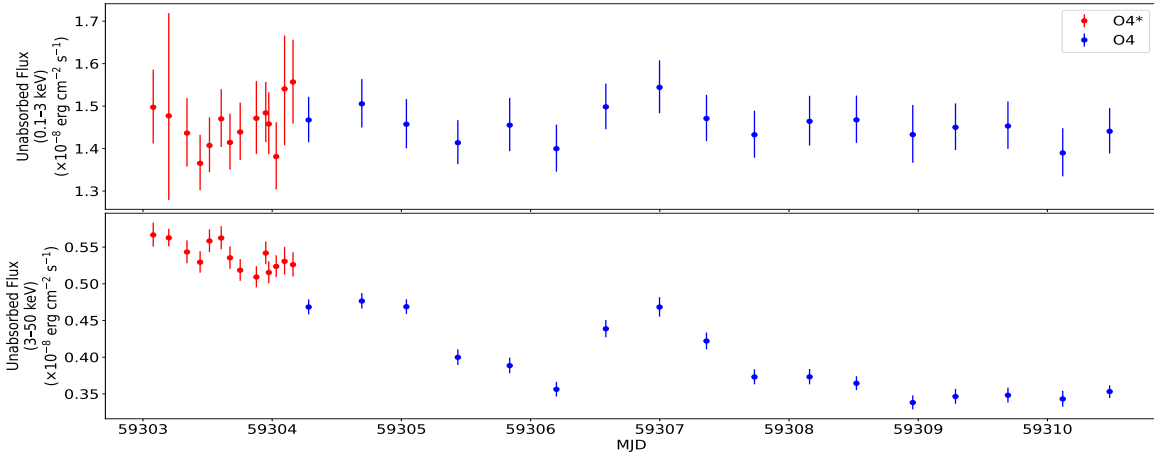

Figure 6. Evolution of unabsorbed flux in the energy range 0.1 - 3 keV (upper panel) and 3 - 50 keV (lower panel) for observations O4* (red) and O4 (blue) as a function of MJD.

spectrum fitting for one of the segments of observation O4 is shown in Figure 4. Offset values after applying the `gain fit` for the energy spectra fitted with **Model 1S** are −0.73 eV, 7.38 eV, and −13.8 eV for observations O1, O2, and O3, respectively. For observation O4*, the offset values range from 5.69 eV to 19.7 eV, while for observation O4, they range from 8.29 eV to 17.2 eV. The best-fit spectral parameters such as photon index, covering fraction, inner disc temperature, and apparent inner disc radius, of all the observations are listed in the Table 2. Figure 5 shows the variation of the spectral parameters during observations O4* and O4. We calculated apparent inner disc radius using the relation `diskbb` normalization (N_{dbb}) = $(R_{in}/D_{10})^2 cos\theta$, where R_{in} is the "apparent" inner disc radius in km, D_{10} is the source distance in units of 10 kpc, and θ is the inclination angle of the disc. We use source distance to be 10 kpc and inclination angle of the disc to be 50° in the calculation of the apparent inner disc radius (Zdziarski et al. 2019). Further, we studied the evolution of unabsorbed flux in the energy range 0.1-3 keV (soft) and 3-50 keV (hard) which is given in Figure 6. The unabsorbed flux is stable in the softer energy range while it decreases in the harder energy range.

3.2 Timing Analysis

We generate PDSs for each observation using `laxpc_find_freqlag`, a routine available in the LAXPC-Software. The PDSs created using this routine are rms normalized, dead time Poisson level and background corrected. We use a time resolution of ~ 6.25 ms and 16,384 bins per segment, resulting in a total segment length of ~ 102.4 s, with the minimum and Nyquist frequencies being ~ 0.01 Hz and ~ 80 Hz, respectively to generate the PDSs in each segment. We observe a peak-like structure in O1, O2, O3, and O4*, but no such feature is observed in O4. In O4*, the PDS shows a broad peak, suggesting a gradual evolution of the QPO centroid frequency over time. To examine the time evolution of the QPO, we divide O4* into fifteen segments of approximately equal duration (~ 2500 − 3000 seconds) as discussed in the Section 2 and generate the PDS for each segment. We also analyze the peak-like feature in the PDS of O1, O2, and O3 but find no significant variation in QPO frequency within the observations. To determine the centroid frequency of the QPOs, we fit the PDSs with the `Lorentzian` model within XSPEC.

During the O1, O2, O3, we observe that the QPO frequency increases from $0.10^{+0.01}_{-0.01}$ Hz in O1 to $0.18^{+0.01}_{-0.01}$ Hz in O2, and further

Photon Index	Covering Fraction	Inner Disc Temp (keV)	R_{in} (km)	χ^2/dof
Observation O1				
$1.55^{+0.01}_{-0.01}$	> 0.97	$0.53^{+0.06}_{-0.07}$	$35.52^{+3.06}_{-6.85}$	133.54/97
Observation O2				
$1.56^{+0.01}_{-0.01}$	$0.95^{+0.03}_{-0.03}$	$0.48^{+0.05}_{-0.05}$	$46.84^{+10.43}_{-8.03}$	113.25/97
Observation O3				
$1.52^{+0.02}_{-0.02}$	$0.59^{+0.08}_{-0.08}$	$0.79^{+0.08}_{-0.09}$	$21.68^{+3.47}_{-2.27}$	88.54/88
Observation O4*				
$2.08^{+0.04}_{-0.04}$	$0.11^{+0.01}_{-0.01}$	$0.82^{+0.02}_{-0.02}$	$54.17^{+4.16}_{-3.58}$	63.41/78
$2.06^{+0.04}_{-0.04}$	$0.11^{+0.01}_{-0.01}$	$0.81^{+0.02}_{-0.02}$	$54.40^{+3.82}_{-3.32}$	96.27/80
$2.07^{+0.04}_{-0.04}$	$0.12^{+0.01}_{-0.01}$	$0.81^{+0.01}_{-0.01}$	$52.66^{+2.49}_{-2.26}$	77.19/85
$2.14^{+0.04}_{-0.04}$	$0.12^{+0.01}_{-0.01}$	$0.83^{+0.01}_{-0.01}$	$50.94^{+2.41}_{-2.19}$	80.40/85
$2.11^{+0.04}_{-0.04}$	$0.12^{+0.01}_{-0.01}$	$0.82^{+0.01}_{-0.01}$	$53.46^{+2.54}_{-2.30}$	82.47/85
$2.16^{+0.04}_{-0.04}$	$0.12^{+0.01}_{-0.01}$	$0.83^{+0.01}_{-0.01}$	$51.70^{+2.46}_{-2.24}$	63.31/85
$2.15^{+0.04}_{-0.04}$	$0.11^{+0.01}_{-0.01}$	$0.82^{+0.01}_{-0.01}$	$52.63^{+2.50}_{-2.28}$	70.19/85
$2.08^{+0.05}_{-0.05}$	$0.08^{+0.01}_{-0.01}$	$0.83^{+0.01}_{-0.01}$	$52.62^{+3.32}_{-2.93}$	72.49/83
$2.15^{+0.04}_{-0.04}$	$0.11^{+0.01}_{-0.01}$	$0.82^{+0.01}_{-0.01}$	$53.57^{+2.60}_{-2.36}$	76.39/85
$2.14^{+0.04}_{-0.04}$	$0.10^{+0.01}_{-0.01}$	$0.82^{+0.01}_{-0.01}$	$52.79^{+2.85}_{-2.55}$	71.74/85
$2.08^{+0.04}_{-0.04}$	$0.10^{+0.01}_{-0.01}$	$0.84^{+0.02}_{-0.02}$	$49.41^{+3.35}_{-2.92}$	64.30/81
$2.10^{+0.04}_{-0.04}$	$0.09^{+0.01}_{-0.01}$	$0.82^{+0.03}_{-0.03}$	$55.34^{+8.05}_{-6.09}$	66.63/73
$2.11^{+0.04}_{-0.04}$	$0.09^{+0.01}_{-0.01}$	$0.81^{+0.02}_{-0.02}$	$56.13^{+5.04}_{-4.21}$	79.29/76
$2.38^{+0.05}_{-0.05}$	$0.12^{+0.02}_{-0.02}$	$0.81^{+0.02}_{-0.02}$	$48.98^{+4.69}_{-3.89}$	71.06/75
Observation O4				
$2.11^{+0.04}_{-0.04}$	$0.07^{+0.01}_{-0.01}$	$0.82^{+0.01}_{-0.01}$	$53.64^{+1.73}_{-1.62}$	67.57/90
$2.09^{+0.04}_{-0.04}$	$0.07^{+0.01}_{-0.01}$	$0.82^{+0.01}_{-0.01}$	$54.68^{+1.83}_{-1.71}$	56.57/89
$2.09^{+0.04}_{-0.04}$	$0.07^{+0.01}_{-0.01}$	$0.82^{+0.01}_{-0.01}$	$52.94^{+2.07}_{-1.89}$	56.31/88
$1.99^{+0.04}_{-0.04}$	$0.04^{+0.01}_{-0.01}$	$0.81^{+0.01}_{-0.01}$	$54.19^{+1.71}_{-1.61}$	54.22/91
$1.95^{+0.04}_{-0.04}$	$0.04^{+0.01}_{-0.01}$	$0.79^{+0.01}_{-0.01}$	$56.78^{+2.29}_{-2.09}$	63.87/87
$1.93^{+0.05}_{-0.05}$	$0.03^{+0.01}_{-0.01}$	$0.79^{+0.01}_{-0.01}$	$55.58^{+1.95}_{-1.83}$	52.72/89
$2.02^{+0.04}_{-0.04}$	$0.05^{+0.01}_{-0.01}$	$0.81^{+0.01}_{-0.01}$	$55.33^{+1.75}_{-1.64}$	58.35/91
$2.11^{+0.04}_{-0.04}$	$0.06^{+0.01}_{-0.01}$	$0.81^{+0.01}_{-0.01}$	$55.63^{+2.21}_{-2.04}$	77.99/87
$2.04^{+0.05}_{-0.05}$	$0.05^{+0.01}_{-0.01}$	$0.81^{+0.01}_{-0.01}$	$54.64^{+1.77}_{-1.67}$	56.77/90
$1.94^{+0.05}_{-0.05}$	$0.03^{+0.01}_{-0.01}$	$0.80^{+0.01}_{-0.01}$	$55.58^{+1.85}_{-1.74}$	59.02/89
$1.94^{+0.05}_{-0.05}$	$0.03^{+0.01}_{-0.01}$	$0.79^{+0.01}_{-0.01}$	$56.59^{+2.03}_{-1.90}$	60.00/88
$1.86^{+0.06}_{-0.06}$	$0.02^{+0.01}_{-0.01}$	$0.80^{+0.01}_{-0.01}$	$56.34^{+1.76}_{-1.67}$	63.94/92
$1.80^{+0.06}_{-0.06}$	$0.02^{+0.01}_{-0.01}$	$0.80^{+0.01}_{-0.01}$	$55.60^{+2.31}_{-2.13}$	63.23/87
$1.64^{+0.06}_{-0.06}$	$0.01^{+0.01}_{-0.01}$	$0.82^{+0.01}_{-0.01}$	$52.96^{+1.76}_{-1.63}$	59.05/91
$1.69^{+0.06}_{-0.07}$	$0.01^{+0.01}_{-0.01}$	$0.82^{+0.01}_{-0.01}$	$52.85^{+1.74}_{-1.61}$	65.94/91
$1.71^{+0.05}_{-0.05}$	$0.01^{+0.01}_{-0.01}$	$0.82^{+0.01}_{-0.01}$	$52.00^{+1.91}_{-1.77}$	77.88/89

Table 2. Best-fit spectral parameters for all observations fitted with **Model 1S**. This table shows the values of photon index, covering fraction, inner disc temperature, and the "apparent" inner disc radius (R_{in}) in kilometers with 90% confidence range
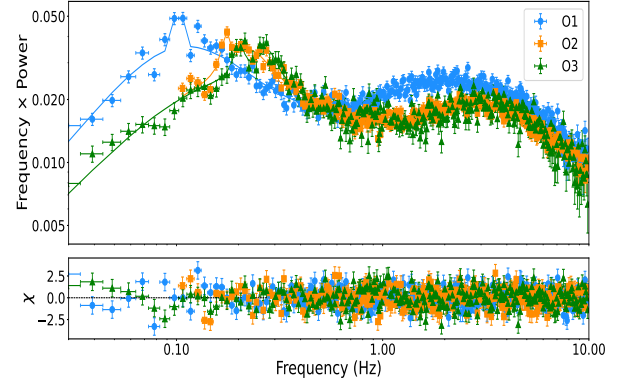
.

Figure 7. Power density spectra (PDS) for the observations O1, O2, and O3. The top panel shows frequency times power ($f \times P(f)$) vs. frequency (Hz), with blue circles (O1), orange squares (O2), and green triangles (O3). Solid lines represent model fits. Power in the PDSs are rms normalised.

The bottom panel displays residuals (Data − Model)/Error.

to $0.20^{+0.01}_{-0.01}$ Hz in O3 (Figure 7) which is also reported by Aneesha et al. (2024), and Chand et al. (2024). No harmonics or subharmonics are observed during these observations. We observe that the QPOs in these observations have frequencies $\sim 0.1 - 0.2$ Hz, quality factor (Q) ≥ 6, and rms $\geq 3\%$ hence we can classify these QPOs as type C (Casella et al. 2005; Ingram & Motta 2019).

In the O4*, harmonics and subharmonics are observed in some segments, which have been reported in the earlier studies by Aneesha et al. (2024) and Mondal et al. (2023). For these PDS fits, we initially use three Lorentzians, along with a power-law component where the photon index is fixed at 0. The number of Lorentzians is adjusted as needed to account for the presence of harmonics and subharmonics. Figure 8 represents the PDS of seg 2 of O4* fitted with multiple Lorentzians and powerlaw. After fitting PDSs of all the segments of O4*, we observe a clear evolution of the QPO frequency, which decreases from $5.65^{+0.06}_{-0.08}$ Hz to $4.57^{+0.12}_{-0.08}$ Hz over time (Figure 9). In this observation, the QPOs show centroid frequencies of approximately 4.5–5.5 Hz, quality factors ≥ 6 (within 3σ), and rms amplitudes of about 4–8%. Based on the classification criteria discussed by Casella et al. (2005) and Ingram et al. (2009), these QPOs can be best classified as type-B. Peirano et al. (2022) also describe these QPOs as type B in their study using same AstroSat data. Aneesha et al. (2024) also reported QPO frequency $5.37^{+0.06}_{-0.02}$ Hz along with harmonics and subharmonics at $9.38^{+0.33}_{-0.37}$ Hz and $2.86^{+0.08}_{-0.11}$ Hz respectively during the initial phase of O4* and find a decrease in the QPO frequency later in time within this observation. However, they did not study the evolution of the QPO frequency over time with proper segmentation. Mondal et al. (2023) performed the orbit-wise PDSs fitting and reported the decrease in QPO frequency. They also reported harmonics and subharmonics in some of the orbits, not in all.

Further, we study the energy-dependent rms and time lag of the QPO during O4* in the energy range of 3-30 keV. For this purpose, we use a subroutine provided by the AstroSat team, laxpc_find_freqlag, which takes characteristic frequency features (ν_0) and frequency resolution ($-l$) as input, along with energy bands and GTI, to compute time lags and rms. Typically, we provide the QPO frequency as ν_0 and $-l$ depends on the total length of the time series. We use the 5.0-7.0 keV energy band as a reference for estimating the time lags (Figure 10).
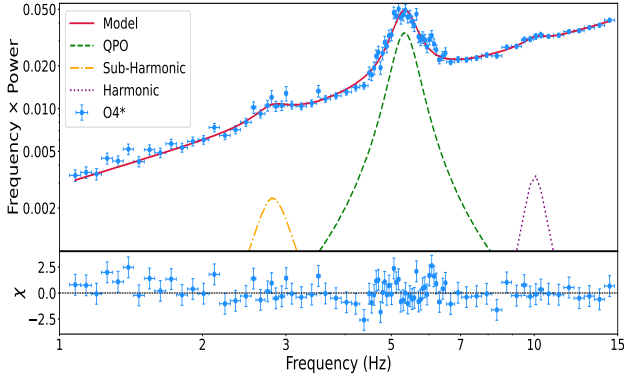
Figure 8. Power density spectrum (PDS) of the observation O4*. The **upper panel** shows the PDS, fitted with multiple **Lorentzian** components and a **power-law**. Blue points represent frequency × power, while the solid red line indicates the best-fit model. Power in the PDS is rms normalised. The **lower panel** displays the residuals (χ values) as green points.
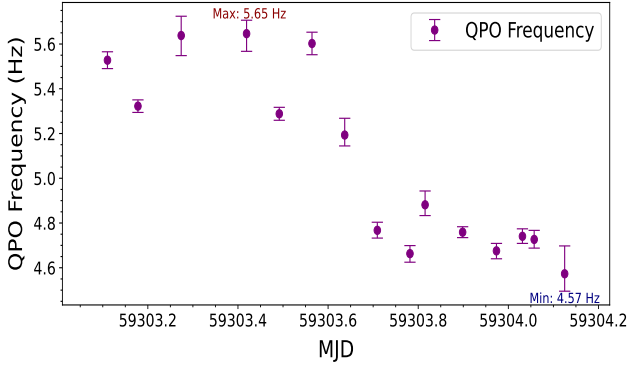

Figure 9. QPO Evolution: The y-axis represents the QPO frequency, while the x-axis shows the modified julian date (MJD). The QPO frequency evolves from approximately 5.7 Hz to 4.5 Hz over time.

We observe that the time lag and rms increase in most of the segments with energy, which has been reported by Mondal et al. (2023) in their orbit-wise analysis.

4 MODELLING RMS AND LAG

Garg et al. (2020) discuss a generic scheme to model the energy-dependent rms and time lags to identify the radiative components responsible for the QPOs observed in XRBs. In this scheme, they assumed that the energy spectrum of BHXBs consists of two components: a thermal and a non-thermal component, which can be modeled by `diskbb` and `nthcomp` within `XSPEC`. They prefer using physical and geometrical parameters over phenomenological spectral parameters. For example, they convert the coronal electron temperature (kT_e), a spectral parameter of `nthcomp`, into the coronal heating rate ($\dot{H}$). Specifically, following the formulation of Garg et al. (2020), $\dot{H}$ is evaluated using the integral:

$$\dot{H} = \int E \left[f \cdot F_c(E, kT_e, \tau) - f \cdot F_d(E, kT_{in}) \right] dE, \quad (1)$$

where $F_c(E)$ is the photon flux from the corona, $F_d(E)$ is the disc

flux, and f is the covering fraction from the `Thcomp` model, representing the disk photons undergoing Comptonization in the corona. The integrand in Equation 1 multiplies the photon flux difference by photon energy E, thereby converting the photon flux into an energy flux. Equation 1 is used to calculate the $\dot{H}$ corresponding to the best-fit spectral parameters obtained from the time-averaged spectral fitting, including the kT_e, kT_{in}, and optical depth (τ).

In the modeling of the energy-dependent rms and time lag spectra, $\dot{H}$ is treated as the variable physical parameter. For each input value of $\dot{H}$, the model iteratively adjusts kT_e until the computed Comptonized spectrum satisfies Equation 1. In this way, the kT_e is used to calculate the $\dot{H}$. This scheme calculates the `first-order variation` in the photon spectrum caused by small changes in the physical parameters using the equations discussed in Garg et al. (2020).

We use the methodology discussed in Garg et al. (2022) to model the energy-dependent time lags and rms. Garg et al. (2022) modify the model discussed in Garg et al. (2020) and replace `nthcomp` with `thcomp` to fit the energy spectrum. We fit the energy spectrum of all the segments with the XSPEC model **constant × tbabs × (gaussian + thcomp × diskbb)** as discussed in Section 3.1. As described in Garg et al. (2022), we freeze all the spectral parameters to the best-fit values and replaced `thcomp` with the `thcompph` model, which converts the kT_e into the physical parameter, $\dot{H}$. We keep $\dot{H}$ free and fit the spectrum to obtain its best-fit value.

After fitting the energy spectra of all the segments with the model **constant × tbabs × (gaussian + thcompph × diskbb)**, as prescribed by the scheme, we proceed to fit the time lag and rms spectra using the model discussed in Garg et al. (2020) and Garg et al. (2022). We begin by considering variations in the disc temperature ($|\delta kT_{in}|$) and heating rate ($|\delta\dot{H}|$), with a phase-lag $\phi_{\dot{H}}$ between them. We refer to this as **Model 1T** (Figure 10). However, we are unable achieve a good fit for most of the segments, as we observe reduced $\chi^2 > 2$ (Figure 11)

To improve the fit, we introduce one more variation in terms of disc normalization ($|\delta N_{disc}|$) and a phase-lag $\phi_{N_{disc}}$ between $|\delta N_{disc}|$ and $|\delta kT_{in}|$. This model is refer to as **Model 2T**. With this model fitting, we observe that phase-lag $\phi_{\dot{H}}$ is zero between $|\delta\dot{H}|$ and $|\delta kT_{in}|$, hence we freeze it at zero. The introduction of $|\delta N_{disc}|$ improves the model fit for most segments (Figure 12), with χ^2_{red} found to be less than 1 in most of the segments (Figure 11).

5 DISCUSSIONS AND CONCLUSIONS

We study the spectral and temporal properties of the BH LMXB GX 339-4 using *AstroSat*'s LAXPC and SXT data during its 2021 outburst. After dividing the data into multiple segments as discussed in Section 3.1, we fit the energy spectrum with Model 1S: **constant × tbabs × (gaussian + thcomp × diskbb)**, assuming that the energy spectrum of the BH LMXB consists primarily of two components: a thermal component and a non-thermal component. This model provided a good fit (Figure 3 & 4).

We observe the photon index to be $1.55^{+0.01}_{-0.01}$, $1.56^{+0.01}_{-0.01}$, and $1.52^{+0.02}_{-0.02}$ during the observations O1, O2, and O3, respectively, indicating a relatively hard spectral state in these observations. In contrast, during the observation O4*, the photon index remained steady around ~ 2.11, suggesting a transition to a softer state. However, during the observation O4, the photon index decreased from $2.11^{+0.04}-0.04$ to $1.71^{+0.05}_{-0.05}$ (Figure 5), pointing toward spectral hardening during this time. The covering fraction also showed significant changes across observations. It is quite high during O1 and O2, with values > 0.93 and $0.95^{+0.04}_{-0.04}$ respectively, and moderately lower in
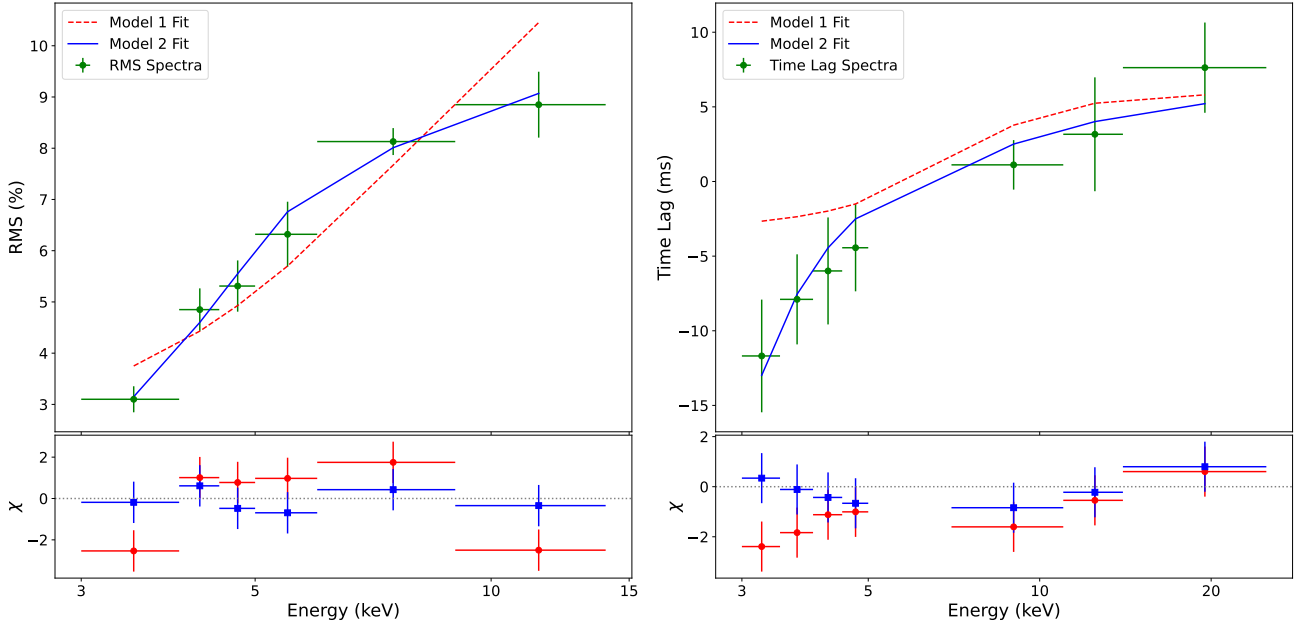
Figure 10. The RMS and time-lag spectra fitted with **Model 1T** and **Model 2T** discussed in Section 4. Green data points in the upper left panel represent the rms in percentage while that in upper right panel represent the time lag (ms). Dashed red and blue line represent the model 1T and model 2T fitting. The lower panel of both left and right panel display the χ corresponding to model 1T and model 2T fitting with red and blue data points, respectively. We use the $5 - 7$ keV energy band as a reference to calculate the time lag spectra.
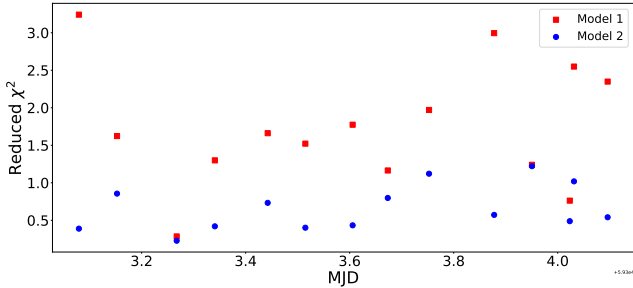

Figure 11. Reduced χ^2 observed in different segments after fitting the rms and time-lag spectra with **Model 1T** (Red) and **Model 2T** (Blue)

O3 at $0.62^{+0.08}-0.08$. In contrast, the covering fraction dropped to very low values during both O4* (below 0.14) and O4 (below 0.08), with a clear declining trend across O4 (Table 2 & Figure 5).

The inner disc temperature vary between 0.46 and 0.87 keV during the observations O1–O3, but remain stable around ~ 0.82 keV throughout both O4* and O4. Interestingly, we find that the apparent inner disc radius to be lower during O1–O3 (HIMS) compared to O4* and O4, which is somewhat unexpected. One possible explanation for this discrepancy could be a change in the color correction factor between these states. To explore this further, we added an additional warm Comptonization component (`thcomp`) to our base model (Model 1S). With this updated model, we found that the upper bound of the `diskbb` normalization become unconstrained, which supports the idea that the true inner disc radius might be larger than previously estimated. In O4* and O4, the inner radius remained stable at around ~ 55 km, showing small variation within the uncertainties. These results are also reflected in the broadband flux behavior. As shown

in Figure 6, the soft X-ray flux (0.1–3 keV) remains mostly constant, consistent with the small variation in disc parameters (e.g., kT_{in} and R_{in}). On the other hand, the hard X-ray flux (3–50 keV) declines with time, likely driving the changes observed in the HID during O4* and O4 (Figure 2).

Furthermore, we observe the QPOs in all the observations except O4. We fit the PDS with multiple **Lorentzians** along with a **power law** component, keeping the photon index fixed at 0. We observe harmonics and subharmonics in some segments of O4*, but not in all. During O1, O2, and O3, we observe a steady increase in the QPO frequency, rising from 0.10 Hz in O1 to 0.18 Hz in O2, and further to 0.20 Hz in O3, which is earlier reported by Aneesha et al. (2024), and Chand et al. (2024). Notably, no harmonics or subharmonics are detected during these observations. In contrast, during O4*, harmonics and subharmonics are observed in some segments. A clear evolution in the QPO frequency is observed in this observation, with the frequency gradually decreasing from ~ 5.65 Hz to ~ 4.57 Hz over time (Figure 9). Mondal et al. (2023) also reported the gradual decrease in the QPO frequency in their orbit-wise analysis, as well as harmonics and subharmonics in a few orbits. Our spectral and temporal analysis suggest that the source remains in the HIMS during the first three observations (O1, O2, and O3), and subsequently transitions to the SIMS during the eight-day observation. Specifically, in observations O1, O2, and O3, we measure a photon index of ~ 1.5 (Table 2) along with the presence of type-C QPOs (Figure 7), which are the characteristic of the HIMS (Homan & Belloni 2005). In contrast, during observations O4* and O4, the photon index increases to ~ 2 (Table 2), accompanied either by type-B QPOs (figure 8) or by the absence of QPOs, consistent with the SIMS (Homan & Belloni 2005).

Further, we study the **rms** and **time lag** spectra of the observed QPOs in O4*, and we observe that the rms increased with energy as reported by (Mondal et al. 2023). A similar increasing trend is observed for the time lags, which exhibits hard lags. Peirano et al.
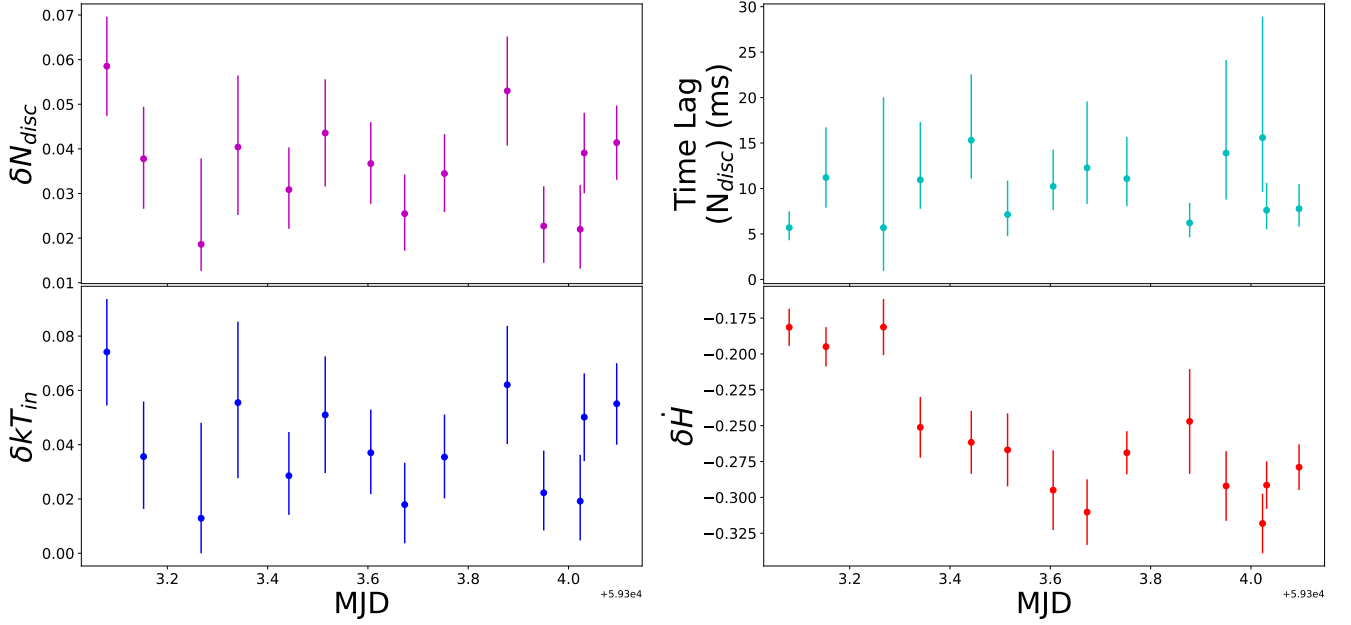
Figure 12. Observed variations in different spectral parameters after fitting the rms and time lag spectra with **Model 2T**. The observed variations in disc normalization, and inner disc temperature in different segments are shown in the upper, and lower panels of the left column, respectively. The time lag between disc normalization and disc temperature, and the observed variation in heating rate are shown in the upper, and lower panels of the right column, respectively.

(2022) studied the rms and lag spectra of the type B QPO utilizing initial exposure of O4* and NICER. They used time-dependent Comptanization models VKOMPTH and VKDUALDK (see for Bellavita et al. 2022 model details and references therein) to fit the simultaneous rms and lag spectra of the type B QPO and energy spectra of the GX 339-4. They require two physically-connected Comptonization regions to explain the radiative properties of the QPO. However, these models considers only the Compton scattering time-scale, which in general led to very large coronal sizes. Previous studies, such as Ma et al. (2023), Rawat et al. (2023), Rout et al. (2023), Bellavita et al. (2025), reported coronal size $> 10^3$ km using this model, which is larger than expected. Peirano et al. (2022) also reported very large coronal size of ~ 18000 km along with smaller corona with a size of ~ 300 km, and later they suggest the geometry of corona to be cylindrical rather than spherical which is the assumed geometry of this model. While Garg et al. (2020) assume the propagation delays between the disk and coronal variations and attempts to understand which radiative components, and in particular, the variation of which physical parameter, can model the observed rms and lag spectra of the QPO. The scheme has successfully described the milli-seconds time delays for low-frequency QPOs and broad features for several BHXBs (for e.g. Garg et al. 2022; Hussain et al. 2023; Tanenia et al. 2024; Dhaka et al. 2024; Pradhan et al. 2025) while considering variations in the spectral parameters in most of the cases. Thereby, in this work, we intend to investigate whether such correlated variations between the disk and corona can also describe the variability features observed in the GX 339-4.

Garg et al. (2020) demonstrated the application of this model to type C QPOs and their harmonics observed in GRS 1915+105. Their results suggest that the energy-dependent features of the QPOs can be explained by variations in the kT_{in}, R_{in}, $\dot{H}$, and τ, with short time delays between these parameters. Garg et al. (2022) apply the same model to type C QPOs observed in MAXI J1535–571. They find hard lags for QPO frequencies below 2 Hz and soft lags for

frequencies above 2 Hz. Their results indicate that for QPOs with frequencies < 2 Hz (hard lags), the variability originates in the disc and propagates inward towards the corona with millisecond time delays, whereas for the QPOs with frequencies > 2 Hz (soft lags), the variations likely originate in the corona and then propagate outward towards the disc. Hussain et al. (2023) use this model to explore the radiative components responsible for the observed QPO and its harmonic in H 1743–322. Their findings are broadly consistent with earlier studies, showing that for the harmonic (associated with hard lags), the variations start in the disc and propagate inward towards the corona, while for the fundamental QPO (showing soft lags), the variability originates in the inner hot flow and propagates outward towards the disc. More recently, Pradhan et al. (2025) applied this model to explain broad features, type C, and type B QPOs observed in MAXI J1803–298 across different spectral states, again reporting consistent results. Similarly, Dhaka et al. (2024) and Tanenia et al. (2024) used this model to interpret the broad features observed in the PDS of GRS 1915+105 and GX 339–4, respectively. Dhaka et al. (2024) report soft lags, while Tanenia et al. (2024) find hard lags, both supporting the same physical scenario inferred from the previous applications of this model.

We begin to fit the rms and time lag spectra of the observed type B QPOs during O4* by introducing the first-order variations in the inner disc temperature ($|\delta kT_{in}|$) and heating rate ($|\delta\dot{H}|$), with a phase-lag ϕ_H between them (Model 1T), but we can not adequately fit the rms and lag spectra (Figure 10 & 11). By introducing an additional variation in the disc normalization ($|\delta N_{disc}|$) and a phase-lag $\phi_{N_{disc}}$ with respect to $|\delta kT_{in}|$ (Model 2T) (Figure 10), we reproduce the energy-dependent properties of the QPOs in most segments (Figure 12) with a X^2_{red} close to 1 (Figure 11). From Figure 12, it is evident that the variations in kT_{in} are positive while those in $\dot{H}$ are negative with a phase lag zero. This indicates that when kT_{in} increases by δkT_{in}, $\dot{H}$ decreases by $\delta\dot{H}$. Therefore, we observe that simultaneous variations in the kT_{in}, and $\dot{H}$ are the primary driver of the observed

variability, while they are anti-correlated and after a ~ 10 ms of time delay, these variations propagate to vary the N_{dbb} parameter (Figure 12). Hence, we could also reproduce rms and lag spectra by introducing some variations in the disc and coronal parameters same as previous studies, however our results suggest that the variability originates in the the kT_{in}, and $\dot{H}$ simultaneously which then propagate to N_{dbb} for the observed hard lags though previous studies reported variations get originated in the disc and propagate inwards towards the corona with some time delay. Although this model of Garg et al. (2020) represent the simplest picture of the complex phenomenon, it is remarkable that we as well as previous studies can fit the rms and lag spectra of the observed QPOs by just introducing first order variations in the spectral parameters. More studies in future like we present in this work, by applying this model to BHXBs, may give us better understanding about the role of radiative components in the energy-dependent features of the QPOs observed in BHXBs. Furthermore, in this analysis, we do not include reflection components for simplicity, as the applied model does not currently account for reflection effects. Incorporating reflection features into the model could provide a more complete understanding of the physical processes involved, highlighting the need for future model developments to include such complex spectral components.

In this work, we conducted a spectral and temporal study of the BHXB GX 339-4 during its 2021 outburst, and our key findings are as follows:

(i) We fit the combined energy spectrum of SXT and LAXPC in the energy range $0.7 - 25.0$ keV with **constant $\times$ tbabs $\times$ (gaussian + thcomp $\times$ diskbb)** (Model 1S) and assuming that the energy spectrum of BH LMXBs primarily consists of two components: a thermal component and a non-thermal component.

(ii) The spectrum gets harder during O4, as we see the photon index and covering fraction both decreasing. Interestingly, the disc doesn't change much since its temperature and apparent inner radius remain same, which is also confirmed by the stable unabsorbed flux in 0.1-3 keV energy range.

(iii) Even though the soft X-ray flux stays steady, the hard X-ray flux keeps dropping, which suggests the corona is weakening over time. This likely explains the changes we see in the HID during O4* and O4.

(iv) Study of the X-ray variability in the frequency domain through the PDS suggests that the QPO frequency increases from ~ 0.10 Hz in O1 to ~ 0.18 Hz in O2, and further to ~ 0.20 Hz in O3, and decreases from ~ 5.7 Hz to ~ 4.5 Hz during O4*.

(v) The rms of the QPO frequencies observed in the observation O4* increases with the energy and the lag spectra indicate the hard lags.

(vi) To investigate the radiative component responsible for the observed QPO, we employ the generic scheme discussed in Garg et al. (2020) and Garg et al. (2022) to fit the rms and time lag spectra. We successfully reproduce the energy-dependent rms and time lag (Figure 10). Interestingly, we find that the variations originate simultaneously in the inner disc temperature (kT_{in}) and the heating rate ($\dot{H}$); however, they are anti-correlated (Figure 12). After a time delay of ~ 10 ms, these variations propagate to the disc normalization (N_{dbb}).

DATA AVAILABILITY

The data used in this study is publicly available through the Indian Space Science Data Centre (ISSDC), which serves as the primary repository for the *AstroSat* mission. Researchers can access the data via the ISSDC's AstroBrowse platform at http://astrobrowse.issdc.gov.in/astro_archive/archive.

REFERENCES

Agrawal P. C., Yadav J. S., Antia H. M., et al., 2017, Journal of Astrophysics and Astronomy, 38, 30
Alabarta K., et al., 2021, MNRAS, 507, 5507
Aneesha U., Das S., Katoch T. B., Nandi A., 2024, Monthly Notices of the Royal Astronomical Society, 532, 4486
Antia H. M., Yadav J. S., Agrawal P. C., et al., 2017, The Astrophysical Journal Supplement Series, 231, 10
Antia H. M., et al., 2021, Journal of Astrophysics and Astronomy, 42, 32
Arzoumanian Z., et al., 2014, in Takahashi T., den Herder J.-W. A., Bautz M., eds, Society of Photo-Optical Instrumentation Engineers (SPIE) Conference Series Vol. 9144, Space Telescopes and Instrumentation 2014: Ultraviolet to Gamma Ray. p. 914420, doi:10.1117/12.2056811
Bellavita C., García F., Méndez M., Poutanen J., Veledina A., 2022, Monthly Notices of the Royal Astronomical Society, 515, 2099
Bellavita C., Méndez M., García F., Ma R., König O., 2025, A&A, 696, A128
Belloni T., Psaltis D., van der Klis M., 2002, The Astrophysical Journal, 572, 392
Belloni T., Homan J., Casella P., et al. 2005, Astronomy & Astrophysics, 440, 207
Belloni T. M., Sanna A., Méndez M., 2012, Monthly Notices of the Royal Astronomical Society, 426, 1701
Bhuvana G. R., Radhika D., Nandi A., 2021, The Astronomer's Telegram, 14455, 1
Casella P., Belloni T., Stella L., 2005, ApJ, 629, 403
Chakrabarti S., Titarchuk L. G., 1995, The Astrophysical Journal, 455, 623
Chakrabarti S. K., Debnath D., Nandi A., Pal P. S., 2008, Astronomy & Astrophysics, 489, L41
Chand S., Dewangan G. C., Zdziarski A. A., Bhattacharya D., Mithun N. P. S., Vadawale S. V., 2024, The Astrophysical Journal, 972, 20
Deegan P., Combet C., Wynn G. A., 2009, Monthly Notices of the Royal Astronomical Society, 400, 1337
Dhaka R., Misra R., Jain P., Yadav J. S., 2024, The Astrophysical Journal, 974, 90
Done C., Gierliński M., Kubota A., 2007, A&ARv, 15, 1
Dubus G., Hameury J. M., Lasota J. P., 2001, Astronomy & Astrophysics, 373, 251
Fabian A. C., Rees M. J., Stella L., White N. E., 1989, Monthly Notices of the Royal Astronomical Society, 238, 729
Garcia J., Tomsick J., Harrison F., Connors R., Mastroserio G., 2021, The Astronomer's Telegram, 14352, 1
Garg A., Misra R., Sen S., 2020, Monthly Notices of the Royal Astronomical Society, 498, 2757
Garg A., Misra R., Sen S., 2022, Monthly Notices of the Royal Astronomical Society, 514, 3285
Gendreau K. C., et al., 2016, in den Herder J.-W. A., Takahashi T., Bautz M., eds, Society of Photo-Optical Instrumentation Engineers (SPIE) Conference Series Vol. 9905, Space Telescopes and Instrumentation 2016: Ultraviolet to Gamma Ray. p. 99051H, doi:10.1117/12.2231304

Haardt F., Maraschi L., 1993, The Astrophysical Journal, 413, 507

Harrison F. A., Craig W. W., Christensen F. E., Hailey C. J., Zhang W. W., Boggs S. E., Stern D., et al., 2013, ApJ, 770, 103

Heida M., Jonker P. G., Torres M. A. P., Chiavassa A., 2017, The Astrophysical Journal, 846, 132

Homan J., Belloni T., 2005, Ap&SS, 300, 107

Homan J., Wijnands R., van der Klis M., Belloni T., van Paradijs J., Klein-Wolt M., Fender R., Méndez M., 2001, ApJS, 132, 377

Husain N., Mudambi S. P., Garg A., Misra R., Sen S., Maqbool B., 2021, The Astronomer's Telegram, 14400, 1

Hussain N., Garg A., Misra R., Sen S., 2023, Monthly Notices of the Royal Astronomical Society, 525, 4515

Hynes R. I., Steeghs D., Casares J., Charles P. A., O'Brien K., 2003, ApJ, 583, L95

Ingram A. R., Motta S. E., 2019, New Astronomy Reviews, 85, 101524

Ingram A., Done C., Fragile P. C., 2009, Monthly Notices of the Royal Astronomical Society, 397, L101

Jana A., Chatterjee D., Chang H.-K., Naik S., Mondal S., 2024, Monthly Notices of the Royal Astronomical Society, 527, 2128

Kaastra J. S., Bleeker J. A. M., 2016, A&A, 587, A151

Karpouzas K., Méndez M., García F., Poutanen J., Veledina A., 2020, Monthly Notices of the Royal Astronomical Society, 492, 1399

Liu H., Ji L., Bambi C., Jain P., Misra R., Rawat D., Yadav J., Zhang Y., 2021, The Astrophysical Journal, 909, 63

Ma R., Méndez M., García F., Sai N., Zhang L., Zhang Y., 2023, MNRAS, 525, 854

Maqbool B., Mudambi S. P., Misra R., Yadav J. S., Jain P., 2019, Monthly Notices of the Royal Astronomical Society, 486, 2964

Markert T. H., Canizares C. R., Clark G. W., et al. 1973, The Astrophysical Journal Letters, 184, L67

Matt G., Perola G. C., Piro L., 1991, Astronomy & Astrophysics, 247, 25

Misra R., Mandal S., 2013, The Astrophysical Journal, 779, 71

Mitsuda K., Inoue H., Koyama K., et al., 1984, Publications of the Astronomical Society of Japan, 36, 741

Mondal S., Salgundi A., Chatterjee D., Jana A., Chang H.-K., Naik S., 2023, Monthly Notices of the Royal Astronomical Society, 526, 4718

Motta S. E., Casella P., Henze M., Mu noz-Darias T., Sanna A., Fender R., Belloni T., 2015, MNRAS, 447, 2059

Motta S. E., Belloni T., Stella L., Pappas G., Casares J., Muñoz-Darias T., Torres M. A. P., Yanes-Rizo I. V., 2022, Monthly Notices of the Royal Astronomical Society, 517, 1469

Méndez M., Altamirano D., Belloni T., Sanna A., 2013, Monthly Notices of the Royal Astronomical Society, 435, 2132

Nowak M. A., 2000, Monthly Notices of the Royal Astronomical Society, 318, 361

Parker M. L., Tomsick J. A., Kennea J. A., et al. 2016, The Astrophysical Journal Letters, 821, L6

Peirano V., Méndez M., García F., Belloni T., 2022, Monthly Notices of the Royal Astronomical Society, 519, 1336

Pradhan A., Garg A., Misra R., Sarkar B., 2025, ApJ, 991, 93

Rawat D., et al., 2023, MNRAS, 520, 113

Remillard R. A., McClintock J. E., 2006, Annual Review of Astronomy and Astrophysics, 44, 49

Rout S. K., Méndez M., García F., 2023, MNRAS, 525, 221

Shakura N. I., Sunyaev R. A., 1973, Astronomy & Astrophysics, 24, 337

Singh K. P., et al., 2014, in Takahashi T., den Herder J.-W. A., Bautz M., eds, Society of Photo-Optical Instrumentation Engineers (SPIE) Conference Series Vol. 9144, Space Telescopes and Instrumentation 2014: Ultraviolet to Gamma Ray. p. 91441S, doi:10.1117/12.2062667

Singh K. P., Stewart G. C., Chandra S., et al., 2016, in den Herder J.-W. A., Takahashi T., Bautz M., eds, Society of Photo-Optical Instrumentation Engineers (SPIE) Conference Series Vol. 9905, Space Telescopes and Instrumentation 2016: Ultraviolet to Gamma Ray. p. 99051E, doi:10.1117/12.2235309

Singh K. P., Stewart G. C., Westergaard N. J., et al., 2017, Journal of Astrophysics and Astronomy, 38, 29

Sobczak G. J., Remillard R. A., Muno M. P., McClintock J. E., 2000, arXiv e-prints, pp astro–ph/0004215

Sreehari H., Iyer N., Radhika D., Nandi A., Mandal S., 2019, Advances in Space Research, 63, 1374

Stella L., Vietri M., 1997, The Astrophysical Journal, 492, L59

Stella L., Vietri M., Morsink S. M., 1999, The Astrophysical Journal, 524, L63

Tanenia H., Garg A., Misra R., Sen S., 2024, The Astrophysical Journal, 975, 190

Tetarenko B. E., Sivakoff G. R., Heinke C. O., Gladstone J. C., 2016, ApJS, 222, 15

Titarchuk L., Osherovich V., 2000, The Astrophysical Journal Letters, 542, L111

Wang J., et al., 2021, The Astronomer's Telegram, 14384, 1

Wijnands R., Homan J., van der Klis M., 1999, ApJ, 526, L33

Wilms J., Allen A., McCray R., 2000, The Astrophysical Journal, 542, 914

Yadav J. S., Misra R., Verdhan Chauhan J., et al., 2016a, The Astrophysical Journal, 833, 27

Yadav J. S., Agrawal P. C., Antia H. M., et al., 2016b, in den Herder J.-W. A., Takahashi T., Bautz M., eds, Society of Photo-Optical Instrumentation Engineers (SPIE) Conference Series Vol. 9905, Space Telescopes and Instrumentation 2016: Ultraviolet to Gamma Ray. p. 99051D, doi:10.1117/12.2231857

Zdziarski A. A., Ziółkowski J., Mikołajewska J., 2019, Monthly Notices of the Royal Astronomical Society, 488, 1026

Zdziarski A. A., Szanecki M., Poutanen J., Gierliński M., Biernacki P., 2020, Monthly Notices of the Royal Astronomical Society, 492, 5234

Zhang S.-N., et al., 2020, Science China Physics, Mechanics, and Astronomy, 63, 249502

This paper has been typeset from a TEX/LATEX file prepared by the author.